Chapter 1

INTRODUCTION

The past decades have seen enormous advances in the fields of microelectronics, micro mechanics and wireless communications. With these advances have emerged a new array of low-power devices that function in hard-to-reach locations; examples are remote sensors and monitors, medical implants and wireless actuators. Due to the difficulty of accessing these devices' location, introducing power cables is impractical and periodically replacing their batteries poses significant challenges. A strong emphasis has been put into the development of systems that can harvest small amounts of energy from on-site natural resources (Elvin and Erturk, 2013; Lee et al., 2015; Mateu and Moll, 2005; Paradiso and Starner, 2005; Park and Chou, 2006; Weimer et al., 2006). These systems would allow the devices' continuous operation without the need of accessing their location. A promising line of work is the exploitation of ambient vibrations to generate strains in a piezoelectric material, which can, in turn, convert these strains into electric energy (Ahmed et al., 2017; Liu et al., 2018; Priya, 2007; Sodano et al., 2004). In many cases, a reliable source of vibrations is a surrounding flow. Since the early work of Allen and Smits (2001) and Taylor et al. (2001), substantial amounts of research have focused on the flapping motion of flags as a source of vibration for piezoelectric energy harvesters.

The study of the solid-fluid interactions that develop when a flag is immersed in a uniform wind dates back to the work of Rayleigh (1878). Although many theoretical analyses shortly followed, the first experimental investigation of a flapping flag was performed by Taneda (1968). The problem was revisited by Zhang et al. (2000), and many more studies — theoretical, numerical and experimental — have emerged in recent years. Comprehensive reviews of the recent developments can be found at Yu et al. (2019), Shelley and Zhang (2011), Eloy et al. (2008) and Païdoussis (1998). The dynamics of a flag immersed in a uniform flow can be divided into three separate regimes. At low flow speeds, the flag remains at rest and aligned with the flow in what has been denominated the stretched-straight state. In this state, a thin vortex street of alternating signs trails the flag's trailing edge. At a critical velocity, the stability of the stretched-straight mode is lost through flutter and the flag enters a periodic flapping mode. In this regime, the vortex sheet that is shed is comprised of vortices of a single sign, with the sign alternating each half stroke of the flag.

A bi-stable region has been reported, where both stretched-straight and periodic flapping regimes co-exist. As wind speed is further increased the power spectrum of the flag's motion becomes broadband and the flag enters a chaotic flapping mode.

Because the bending stiffness of piezoelectric panels is substantially larger than that of a cloth flag, the piezoelectric flag is analogous to a cantilever plate, and the critical velocity at which the flapping motion is onset is relatively high. One common remedy to this problem is the placement of an upstream bluff body whose vortex street induces vibrations on the flag (Taylor et al., 2001). In Kim et al. (2013) we followed a different approach and proposed an alternate configuration, the inverted flag, where the leading edge of the cantilever is free to move and the trailing edge is clamped. This configuration is unstable at low flow velocities, making it a good candidate for piezoelectric energy harvesters. Additionally, the maximum flapping amplitude of the inverted flag is approximately 1.7 times its length, which is several times higher than the maximum flapping amplitude reported for regular flags. The higher amplitudes impose significantly higher strains on the piezoelectric material, which may increase up to ten times the energy harvesting efficiency of the system (Gurugubelli and Jaiman, 2015).

The inverted flag presents three main dynamical regimes as a function of free stream velocity. They are represented in figure 1.1, where each image has been obtained by superimposing snapshots of the flag's motion. At low velocities, the flag undergoes small amplitude oscillations around the undeflected position in the denominated straight regime. During these oscillations the flow remains attached (Goza et al., 2018; Gurugubelli and Jaiman, 2015). As the flow speed is increased, it reaches a critical value at which the flag becomes unstable, undergoing a large amplitude flapping motion. The shedding frequency of vortex structures is correlated to this flapping motion, with a variety of vortex patterns occurring for different velocities (Goza et al., 2018; Gurugubelli and Jaiman, 2015; Kim et al., 2013; Ryu et al., 2015; Shoele and Mittal, 2016). If the wind speed is further increased, the inverted flag enters the deflected regime, where it oscillates with small amplitude around a high deflection equilibrium. Bi-stable regions are present both in the transition from straight to flapping and from flapping to deflected regimes.

In addition to these three main regimes, Sader et al. (2016a) reported the existence of a chaotic mode, where the flag flaps aperiodically with a broad frequency spectrum, between the periodic flapping and deflected regimes. Numerical studies, which correspond to low Reynolds number flows, have reported additional dynamical
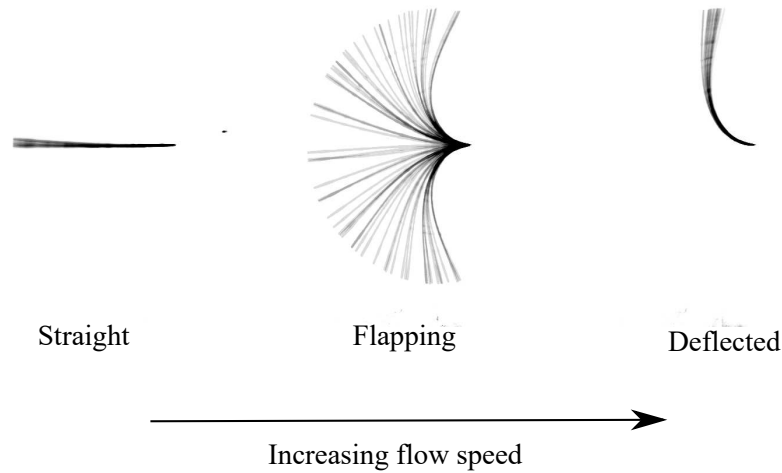
Figure 1.1: Superimposed images of the motion of the inverted flag for the three main dynamical regimes. The flow is left to right and the flags are clamped at their trailing edge.

modes. Ryu et al. (2015) observed the existence of both a small-deflection steady state and a small-deflection small-amplitude flapping regime at flow speeds between those corresponding to the straight and large amplitude flapping regimes. Similar observations have been made by Gurugubelli and Jaiman (2015) and Goza et al. (2018). Gurugubelli and Jaiman (2015) additionally observed a flipped flapping regime at wind speeds higher than those of the deflected regime. In this mode, that has also been observed by Shoele and Mittal (2016) and Tang et al. (2015), the flag bends 180° such that the leading edge is parallel to the flow, recovering a motion similar to that of the conventional flag. Overall, the regimes of motion that have been reported for the inverted flag are, ordered from lowest to highest corresponding flow velocity: straight, small-deflection steady, small-deflection small-amplitude flapping, large amplitude flapping, chaotic, deflected and flipped flapping.

In an attempt to understand the onset of the large amplitude flapping motion, several studies have investigated the loss of stability of the straight regime. While the existence of a divergence instability was hinted by Kim et al. (2013), Gurugubelli and Jaiman (2015) was the first to numerically demonstrate its presence. Sader et al. (2016a) theoretically corroborated the loss of stability of the straight regime through divergence, and provided a simplified analytic formula that reasonably predicts the onset of flapping for inverted flags of aspect ratios higher than 1.

Using a scaling analysis, Sader et al. (2016a) further proved that the flag's flapping motion constitutes a vortex induced vibration. Goza et al. (2018) associated this classic vortex induced vibration with the 2P vortex shedding mode, and linked the appearance of additional shedding modes at higher flow velocities with the breakdown of the VIV and appearance of chaos. The cessation of flapping has received comparably little attention, and is not yet fully understood. Goza et al. (2018) suggested the mechanism behind this transition to be a disruption of lock-on caused by the increased disparity between natural and shedding frequencies of the flag. While the transition velocity from straight to flapping regimes is independent of mass ratio, as defined in Section 1.2, the transition velocity from flapping to deflected regimes decreases as the fluid loading, and therefore damping, increases (Kim et al., 2013), consistent with the lock-off theory.

The results summarized in this section have been obtained for flags with relatively heavy fluid loading; a distinction should be made for flags with light fluid loading. Although these flags still present a flapping mode, this motion does not constitute a vortex induced vibration (Goza et al., 2018). Due to the small thickness of the flag, however, inverted flags are subject to heavy fluid loading for all practical cases.

1.1 Objectives

As has been highlighted above, since it was first introduced in Kim et al. (2013), many advances have been made towards the understanding of the inverted flag's mechanics. However, several aspects that are fundamental for its full characterization are yet to be investigated. The objective of this thesis is to address the most salient of these topics. In many cases, the field has evolved in parallel to the development of this work; recent advances have been addressed in the concluding section of each chapter. This study is predominantly experimental, with some theory being presented to complement the results. Part I of this thesis is organized as follows

- The remainder of Chapter 1 is dedicated to clarifying relevant parameters and definitions and describing the experimental setup employed.

- Chapter 2 researches the dynamics of inverted flags in the limit of very small aspect ratio, which are markedly different to those of the large-aspect-ratio case.

- Chapter 3 addresses the dynamics of inverted flags that are placed at moderate angles of attack to the flow and the modified behavior that arises as this angle
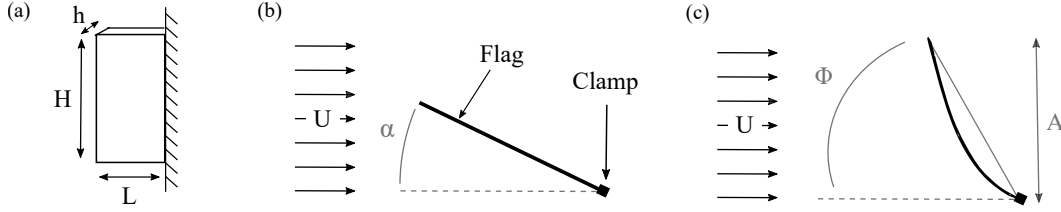
Figure 1.2: Side and top view of the inverted flag with parameters employed to characterize (a) dimensions (H, L and h), (b) angle of attack, α, and (c) deflection, Φ, and amplitude, A

is increased.

- Chapter 4 delves into the behavior of two inverted flags when they are placed in a side-by-side configuration and the interactions and coupling that ensue.

- Chapter 5 concludes the investigation on inverted flags and highlights the most imperative avenues for future work.

1.2 Parameters and definitions

The mathematical description of the inverted flag presented in the literature closely follows that developed for the more general case of an elastic plate with arbitrary boundary conditions (Argentina and Mahadevan, 2005; Kornecki et al., 1976). Accordingly, similar variables and parameters have been introduced to define the inverted flag's behavior. The nomenclature used throughout this thesis is presented hereafter.

The flag's dimensions — length, L, width, H, and thickness, h — have been represented in figure 1.2a. The non-dimensional parameters that determine the behavior of the inverted flag are the angle of attack, α, the non-dimensional velocity, κ, the mass ratio, μ, the aspect ratio, AR, and the Reynolds number, Re. The angle of attack, α, corresponds to the fixed angle of the trailing-edge clamp with respect to the free-stream velocity and is represented in figure 1.2b. The remaining parameters are defined as follows

$$\kappa = \frac{\rho_f U^2 L^3}{D}, \qquad \mu = \frac{\rho_s h}{\rho_f L}, \qquad AR = \frac{H}{L}, \qquad Re = \frac{\rho U L}{\mu_f},$$

where U is the free-stream velocity, ρ_f is the density of the fluid, D the flexural stiffness of the flag ($D = Eh^3/(12(1 - \nu^2))$ with ν the Poisson ratio), ρ_s the density of the flag and μ_f the viscosity of the fluid. The non-dimensional velocity, κ,

represents the ratio of fluid inertial to solid elastic forces, while the Reynolds number, Re, corresponds to the ratio of fluid inertial to fluid viscous forces. The mass ratio, μ, on the other hand, is representative of the relative mass of the flag to that of the fluid it displaces.

The resulting flag's motion is characterized throughout this text using two main parameters, the flag's deflection angle, Φ, and the Strouhal number, St. The deflection angle, Φ, is represented in figure 1.2c and corresponds to the instantaneous angle between the line that joins the flag's leading and trailing edges and the free-stream velocity. Its use differs from previous studies such as Kim et al. (2013) that utilize the amplitude of motion (A, figure 1.2c) as the defining parameter. The choice stems from the non-injectivity of the amplitude of motion: for a given amplitude there are two possible flag positions, one with $\Phi < 90$ and one with $\Phi > 90$. Because a flag can deform under different modes, the deflection angle is not strictly injective either. However, it was experimentally observed that for a given flag at specified flow conditions each deflection angle corresponds to a unique flag position. Variables derived from this parameter, such as the angular amplitude $\Delta\Phi = \Phi_{max} - \Phi_{min}$ and the mean deflection angle, $\bar{\Phi}$, will be employed occasionally. The Strouhal number is defined as follows

$$St = \frac{f A'}{U}$$

where f is the frequency of oscillation and U the free-stream velocity. The cross section A' is calculated as the maximum between $A_{max} - A_{min}$ and $|A_{max}|$, where A_{max} is the maximum amplitude, A_{min} the minimum amplitude and the clamping point is located at A=0. This amplitude corresponds to the cross-flow distance between the shed vortices.

The value of the Reynolds number varies between 10^3 and 10^5 in the experiments presented. The characteristic features of the inverted-flag dynamics and vortex wake have been shown to be fairly insensitive to Reynolds number for $Re > 100$ (Shoele and Mittal, 2016; Tang et al., 2015). For these large Re, the characteristic curves of the flag's motion collapse when represented as a function of κ, independently of flag dimensions, showing that variations with free-stream velocity are a result of the changing behavior with κ and not a Reynolds number effect. For this reason, the effect of Reynolds number has not been analyzed in this study. Similarly, all experiments were performed in air, and although the mass ratio varied due to the

varying flag dimensions its order of magnitude was always $O(1)$. Because such small variations in μ have a negligible effect on the flag's dynamics, the effect of the varying mass ratio has not been considered in this study.

1.3 Experimental setup

The experimental measurements of inverted flags presented in this thesis were performed in an open-loop gust-and-shear wind tunnel constructed at Caltech. A photograph of the experimental setup can be viewed in figure 1.3. The tunnel, similar in design to that of Johnson and Jacob (2009), generates the flow through an array of 10×10 small computer fans. Each row of fans can be controlled individually, allowing for the generation of shear flows, and the fast response of the small fans further allows for the generation of gusts. In this thesis, however, the only flow employed was a uniform steady flow. The tunnel is capable of generating flow speeds between 2.2m/s and 8.5m/s. The variation in the generated free-stream velocity across the tunnel's cross section, caused by the multiplicity of fans, is under 2.7%.

The turbulence intensity at different flow speeds, measured using a hotwire system, is shown in figure 1.4. These intensities are significantly higher than those present in traditional wind tunnels and result in large perturbations to the flag. It is particularly important to consider these perturbations when performing stability analyses; corresponding remarks have been made in the relevant sections of chapters 2 and 3. The control of the individual computer fans is achieved using a pulse-width-modulated signal, resulting in an overshoot of the fan velocity before the steady state is reached. The measurements presented in this manuscript correspond to steady state results — a stabilizing period of at least 30 s was allowed between tunnel velocity modification and recording of data. It is important to note that the inverted flag's motion presents bi-stable regions for certain ranges of the flow velocity. Due to the overshoot when modifying the tunnel's flow velocity, the presence of these regions must be assessed in this setup by modifying the initial conditions of the flag.

The test section of the wind tunnel has a length of 1.9m and a square cross section of $1.2\text{m} \times 1.2\text{m}$. The largest flag tested had dimensions of $0.2\text{m} \times 0.4\text{m}$, resulting in a maximum blockage ratio of 4.7%. No blockage effects were observed in any of the tests performed. The flags were clamped at their trailing edge using two aluminum bars of dimensions $12\text{mm} \times 6\text{mm} \times 1.2\text{m}$. For the study presented in Chapter 4, where a side-by-side flag arrangement is analyzed, two sets of clamping bars were
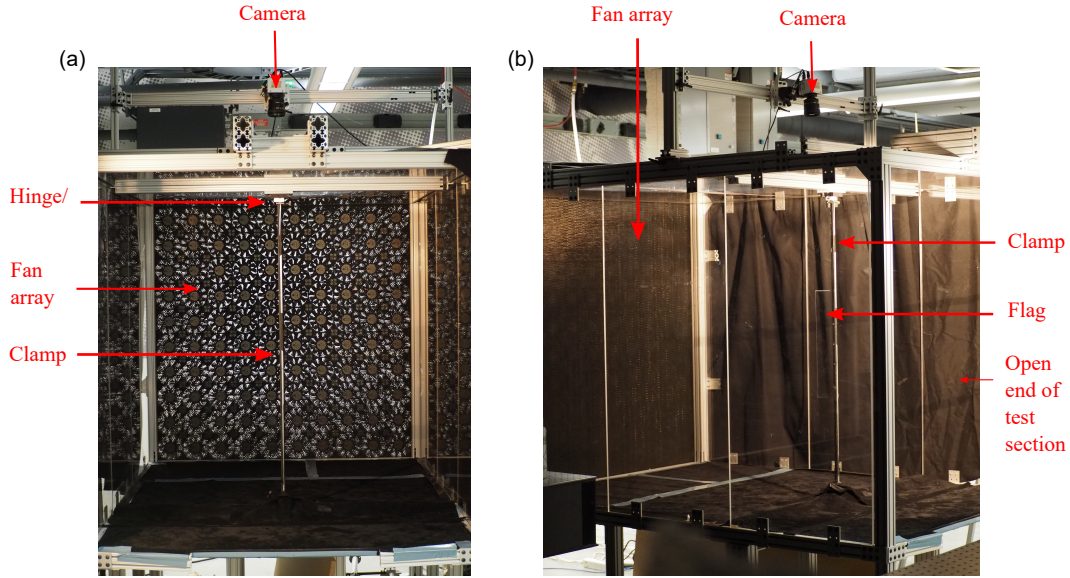
Figure 1.3: Experimental setup from (a) end of test section and (b) side of test section
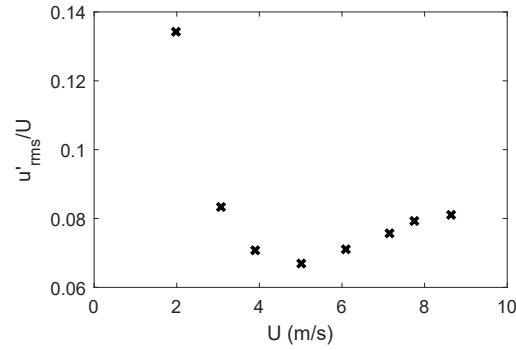

Figure 1.4: Turbulence intensity of the fan array wind tunnel for varying wind speeds

positioned side-by-side and on a rail, such that the distance between flags could be varied. The clamping bars are positioned vertically in the test section to minimize the effect of gravity on the flag dynamics. The deformation of the flag was observed to be two-dimensional in the horizontal plane for the majority of test cases, with the lowest aspect ratio flags being the exception. A discussion of the twisting and the effect of gravity on these flags is presented in Section 2.2. In order to set the desired flag angle of attack, the clamping bars were attached to a hinge that allows rotation around the vertical axis. It is equipped with a dial that shows angles in two-degree increments, resulting in an error in the angle of attack of $\pm 1°$.

Test	Flag number	Dimensions (mm)			AR	μ
		Length	Width	Thickness		
Aspect ratio	1	300	10	0.76	0.033	2.49
	2	300	20	0.76	0.067	2.49
	3	300	30	0.76	0.1	2.49
	4	300	40	0.76	0.13	2.49
	5	195	195	0.51	1	2.55
	6	195	97.5	0.51	0.5	2.55
Angle of attack	7	82	410	0.25	5	3.03
	8	160	320	0.51	2	3.11
	9	180	360	0.51	2	2.76
	10	190	380	0.51	2	2.62
	11	200	400	0.51	2	2.49
Coupling	12	100	150	0.25	1.5	2.48
	13	85	150	0.25	1.76	2.93
	14	90	150	0.25	1.67	2.76
	15	93	150	0.25	1.61	2.68
	16	95	150	0.25	1.58	2.62
	17	98	150	0.25	1.53	2.54
	18	102	150	0.25	1.47	2.44
	19	105	150	0.25	1.73	2.37
	20	107	150	0.25	1.4	2.33
	21	110	150	0.25	1.36	2.26
	22	115	150	0.25	1.3	2.16

Table 1.1: Numbering, dimensions and properties of the inverted flags tested

The motion of the flags was filmed using a high-speed camera (Imperx IPX-VGA210-L or Dantec Dynamics Nanosense MKIII) located above the test section. Images were acquired at frame rates between 20 frames per second and 100 frames per second in sets between 200 and 8,100 frames long. The position of the top edge of the flag, marked with white paint, was tracked in the acquired frames using a MATLAB script. The minimum edge to clamp distance in the acquired images is of 60 pixels and the tracking script was observed to detect the flag edge within four pixels, resulting in errors in the measurement of ϕ smaller than 4°. The dominant frequency of motion of the flag can be subsequently determined making use of the fast Fourier transform of the deflection angle's time series. Measurements of the local deflection angle at the plate's free end were required for a comparison with theoretical results in Chapter 2. They were obtained by fitting a third-order polynomial to the deflected flag shape over the last 20% of the flag length.

The flags consisted of polycarbonate plates with a density of $\rho_s = 1200\text{kg/m}^3$, Young's modulus of $E = 2.41\text{GPa}$ and Poisson ratio of $\nu = 0.38$. A small initial curvature of up to $5°$ was present in the plates due to fabrication and material defects. This curvature was measured experimentally by clamping the flags in the wind tunnel and acquiring images with the fan array turned off. It corresponds to a single mode of deformation; the flags were observed to present similar curvatures in both streamwise and cross-stream directions. Viscoelastic effects in the flag's deformation were only observed for the smallest aspect ratio flags, analyzed in Chapter 2. No time dependence was observed in the deflected stable equilibrium shapes of these flags, confirming that any viscoelastic properties exert a weak effect. Each of the flags used has been assigned a flag number to facilitate identification throughout this text. They are presented, together with their dimensions, aspect ratio and mass ratio, in table 1.1.